An inverse analysis approach based on a POD direct model for the mechanical characterization of metallic materials

M. Bocciarelli [a,*], V. Buljak [b], C.K.S. Moy [c], S.P. Ringer [e,f,g], G. Ranzi [d,e,f]

[a] Architecture, Built Environment and Construction Engineering Department, Politecnico di Milano (Technical University), Piazza Leonardo da Vinci 32, 20133, Italy
[b] University of Belgrade, Faculty of Mechanical Engineering, Department of Strength of Materials, Kraljice Marije 16, Belgrade, Serbia
[c] School of Engineering and Science, Curtin University, Sarawak 98009, Malaysia
[d] School of Civil Engineering, The University of Sydney, Sydney, NSW 2006, Australia
[e] Australian Centre for Microscopy and Microanalysis, The University of Sydney, Sydney, NSW 2006, Australia
[f] ARC Centre of Excellence for Design in Light Metals, The University of Sydney, Sydney, NSW 2006, Australia
[g] School of Aerospace, Mechanical and Mechatronic Engineering, The University of Sydney, Sydney, NSW 2006, Australia

Received 31 January 2014
Received in revised form 10 July 2014
Accepted 11 July 2014
Available online 20 August 2014

1. Introduction

The use of instrumented indentation for the characterization of the material properties for industrial and scientific applications has been gaining popularity in recent years, and current research in this area is focussing, among others, on methodological enhancements, improvements of experimental procedures, and extensions of the applicability of the technique. In the early studies, material properties were estimated by using semi-empirical formulae (see e.g. [1]) that relied on indentation curves relating penetration depths to corresponding imposed forces. More recent developments are based on the processing of the instrumented indentation test results with inverse analysis theory (see e.g. [2–6]). With this approach, the experimental data collected from the instrumented indentation are compared to their computed counterpart by means of a discrepancy function which quantifies the difference between the two. This discrepancy function is then minimized to identify the sought parameters.

Indentation tests combined with inverse analyses have been applied for the mechanical characterization of different classes of materials, namely: isotropic and anisotropic elasto-plastic materials, see e.g. [7–9]; soft materials for biological applications, see e.g. [10,11]; and brittle materials for the identification of fracture properties, see e.g. [12,13].

The difficulty in making use of only indentation curves for the characterization of the elastic modulus, yield stress and strain-hardening parameter was pointed out, among others, by Chen et al. [14], when dealing with mystical materials. These represent a class of materials which exhibit same indentation curves despite having different yield stresses and hardening parameters. Because of this, it is necessary to enrich the experimental information used

* Corresponding author. Tel.: +39 0223994320; fax: +39 0223994369.
E-mail address: massimiliano.bocciarelli@polimi.it (M. Bocciarelli).

in input for the inverse analysis as, for example, carried out by the authors in [15] by including the maximum pile-up height left by the indenter after the test. In Ref. [15], it is shown that this information only is sufficient to make the inverse problem well posed and, therefore, it is not required to measure and consider the whole imprint geometry.

Differently from standard tensile tests, which involve a uniaxial stress–strain field, material properties cannot be inferred directly from the indentation tests, but a mechanical model has to be exploited in combination with the outcomes of the experimental tests to be able to extract quantitative information from these. Despite this, the complex triaxial stress–strain field induced into the material by the indenter penetration represents a material behavior that a standard tensile test cannot capture, and this might become useful when characterizing the properties of components subjected to complex loading conditions, see [16].

In the present paper, the identification of the material parameters is carried out by combining, through inverse analysis, experimental data obtained from the indentation curve and pile-up of the imprint geometry, with a computationally economical, 'a priori' calibrated, finite element model reduction procedure, based on the Proper Orthogonal Decomposition (POD), as described in [17]. The latter is required to avoid the computational demand and possible convergence problems of running standard finite element simulations for the direct analyses.

The efficiency and accuracy of the proposed inverse methodology strictly depend on the efficiency and accuracy of the implemented POD model, whose main drawbacks arise in the calibration stage, where a large number of finite element analyses has to be performed. If the values of the parameters considered in the calibration are distributed regularly over a grid of "nodes" spanning over the parameter space, the number of simulations grows exponentially with the number of sought parameters, with the consequence that the computing time, required to calibrate an accurate POD model, may jeopardize the advantages and the computational efficiency of the whole inverse analysis procedure based on the reduced model. In such cases alternative methods based on randomness should be used, but these approaches require further research.

The approximation of a physical model by means of a model reduction procedure is reliable when the response of the system to external actions is smooth and does not present sudden changes of configuration as, for instance, in fracture mechanics problems, where crack nucleation and propagation represent phenomena which cannot be directly simulated by this approach.

The accuracy of the proposed inverse numerical procedure is finally validated against the measurements obtained from tensile tests, performed on the same materials, highlighting the robustness and adequacy of the adopted approach.

2. Experimental study

The ability of the proposed inverse analysis procedure to identify the mechanical properties of metallic materials is validated against the experimental data collected on samples made of aluminium alloys AA 6061-O and AA 7075-O. In particular, the specimens were cut from metal sheets with thicknesses of 1.55 mm and 1.995 mm for the AA 6061-O and AA 7075-O, respectively. The annealed samples were tested as received without any heat treatment to avoid the influence of precipitation hardening effects [18].

2.1. Mechanical properties according to tensile tests

The material properties of the AA 6061-O and AA 7075-O samples were obtained from standard tensile tests performed in accordance with AS1391-2007 [19]. The measured material parameters are summarised in Table 1, while the corresponding engineering stress–strain curves recorded during the tensile tests are plotted in Fig. 1.

Samples made with AA 6061-O alloy exhibited an average yield stress of 62.9 MPa, with average ultimate strength of 148.6 MPa. In the case of the AA 7075-O samples, mean yield and ultimate stresses observed were 72.7 MPa and 190.5 MPa, respectively. When compared to the AA 6061-O alloy, the AA 7075-O alloy exhibited higher strength and hardening, and a lower level of ductility.

2.2. Indentation tests and imprint mapping

Small samples were cut from the same sheets used for the tensile test specimens and were subjected to indentation tests. The specimens were prepared by carefully polishing them using sequentially grit paper 1200, 6 μm and 1 μm diamond suspension solutions and 0.5 μm silica solution. The micro-indentations were performed on each sample using a 5 μm radius sphero-conical tip on a UMIS 2000 micro-indenter.

The measured indentation load-penetration depth curves are plotted in Fig. 2. The A 6061 alloy samples are quite soft with indentation depths reaching about 7.22 μm, as compared to the AA 7075 specimens with maximum depth in the order of 5.88 μm recorded at the same level of load.

At the completion of each indentation, the maximum heights of the pile-ups were then extracted from the profile mapped with an atomic force microscope (AFM), following a procedure already implemented by the authors in reference [15]. The pile-up heights measured are summarised in Table 2.

3. Inverse analysis based on indentation tests

A computationally efficient inverse analysis procedure was developed and calibrated as part of this study to characterize the mechanical properties of materials, by minimizing the discrepancy between measurable quantities concerning indentation curve and maximum pile-up height, and the corresponding counterparts computed by means of an a-priori calibrated reduced model, based on POD, as a function of the material parameters being estimated. This latter feature of the proposed methodology, as it is illustrated later, allows considerable savings in terms of CPU computing time, with respect to classical inverse analysis procedures.

This approach enabled the estimate of both elastic (modulus of elasticity E) and inelastic (yield stress f_y and exponential hardening coefficient n) parameters. The value of the Poisson's ratio has a negligible influence on the material response in an indentation test (see [2]), and therefore, it was assumed to be known a priori.

The implementation of an inverse analysis based on the indention curve only would be drastically ill-posed, because it is not capable of distinguishing between mystical materials, see e.g. [14,20]. For this reason, an additional measurement, consisting of the maximum pile-up height measured after the indentation test, was used as input for the proposed inverse analysis, similar to a previous work of the authors, see [15], to make the inverse approach well-posed.

In the inverse analysis, the experimental indentation curve was subdivided into T points, including the penetration force $F_i^{\exp}$ and the corresponding indentation depth $u_i^{\exp}$, with $i = 1,2, \ldots ,T$. At the end of the test, the maximum pile-up height $h_{pile-up}^{\exp}$ was also measured. Superscript "exp" highlights that these variables were obtained from the experiments. The finite element model of the test, described in Section 3.1, was used to calibrate the Proper Orthogonal Decomposition (POD) model. This model was then adopted to compute the response of the system to the indentation

Table 1
Mechanical properties related to the nominal stress–strain curves measured from the tensile tests performed in accordance with reference [19].

Sample	Coupon ID	Elastic modulus, E (MPa)	Yield stress, f_y (MPa)	Ultimate stress, f_u (MPa)	Strain hardening exponent, n
AA 6061-O	6061-1	83,104	63.2	148.8	0.179
	6061-2	88,051	62.7	150.6	0.180
	6061-3	86,721	62.9	146.4	0.181
	Average	85,959	62.9	148.6	0.180
AA 7075-O	7075-1	60,176	72.9	189.1	0.209
	7075-2	61,088	73.1	191.4	0.210
	7075-3	64,072	72.2	191.0	0.210
	Average	61,779	72.7	190.5	0.210

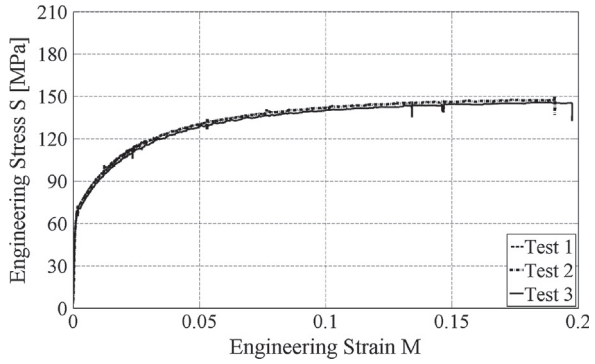

(a) AA 6061-O

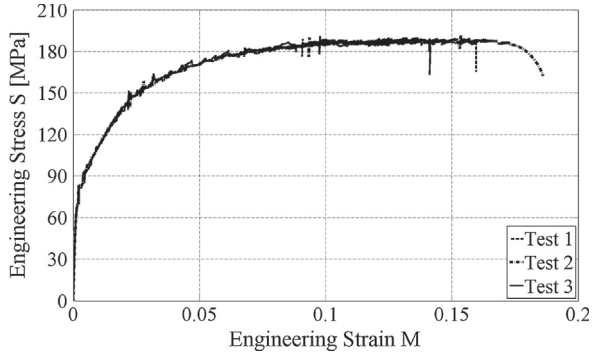

(b) AA 7075-O

Fig. 1. Nominal stress–strain curves measured from experimental tensile tests for the A 6061-O and A 7075-O alloy samples.

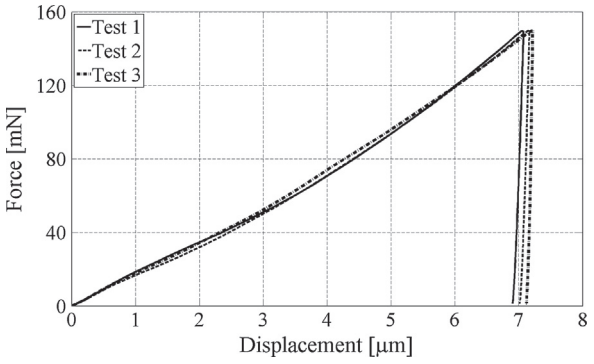

(a) AA 6061-O

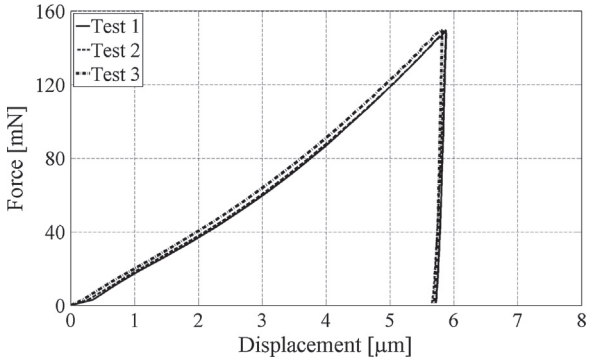

(b) AA 7075-O

Fig. 2. Indentation (load – penetration depth) curves measured using micro-indentation for the A 6061-O and A 7075-O alloy samples.

test in terms of indentation curve $u_i^{com}(\mathbf{p})$ at given force F_i, and maximum pile-up height $h_{pile-up}^{com}(\mathbf{p})$ on varying of the material parameters $\mathbf{p}$ within the iterative minimization procedure. The computed quantities are denoted by superscript "com". The actual values of these quantities were function of the material parameters to be estimated, i.e. elastic modulus, yield stress and exponential hardening coefficient, collected in vector $\mathbf{p}$.

The conventional deterministic batch approach was adopted to minimize the discrepancy function, as in Refs. [21,22], and the uncertainties which affect both the measurements and the system modelling were not processed stochastically. The discrepancy between experimental and computed quantities was defined as follows:

$$\omega(\mathbf{p}) = w_1 \left[\frac{\mathbf{u}^{com}(\mathbf{p}) - \mathbf{u}^{\exp}}{u_{\max}^{\exp}}\right]^T \left[\frac{\mathbf{u}^{com}(\mathbf{p}) - \mathbf{u}^{\exp}}{u_{\max}^{\exp}}\right] + w_2 \left(\frac{h_{pile-up}^{com}(\mathbf{p}) - h_{pile-up}^{\exp}}{h_{pile-up}^{\exp}}\right)^2 \quad (1)$$

Table 2
Maximum pile-up heights left on the samples at the completion of the indentation tests.

	Maximum heights of the pile-up (μm)			
	1	2	3	Mean value
AA 6061-O	0.80	0.86	0.89	0.85 μm
AA 7075-O	0.59	0.56	0.50	0.55 μm

where each term was normalized with respect to the corresponding maximum measured value, i.e. $u_{\max}^{\exp}$ and $h_{pile-up}^{\exp}$. The two parameters w_1 and w_2 (assumed equal to $w_1 = 1$ and $w_2 = 2$, respectively) are weights which were introduced to enable the two sources of errors, depicted in the two terms of Eq. (1), to be numerically comparable. As already shown in Ref. [15], the overall procedure leads to a successful identification of the material parameters if the source of errors introduced by the two terms of Eq. (1) remains within one order of magnitude from each other.

This minimization was performed by the first order Trust Region (TR) algorithm, see e.g. [23], available in conventional optimization tools [24], which started from an initial choice $\mathbf{p}$ of the material parameters and was then automatically updated by an iterative procedure based on subsequent evaluations of the objective function $\omega(\mathbf{p})$ and of its gradient. This process was terminated when either the variation of $\omega(\mathbf{p})$ in two subsequent iterations was less than 2×10^{-8}, or the Euclidean norm of the variation of normalized values of the optimization variables became smaller than 2×10^{-4}.

Since the objective function $\omega(\mathbf{p})$ defined in Eq. (1) is non-linear and non-convex, the inverse problem had to be solved for each set of experimental data many times starting from different initialization vectors to avoid the convergence of the algorithm to a local minimum. In this study, these initializations were uniformly distributed over the parameter domain of interest and the final identified value $p_{i,id}$, for each i sought parameter, was computed as the average of the identified values $p_{ij,id}$ for each initialization j ($j = 1 \ldots K$) weighted with respect to the inverse of the objective function value in solution ω_j:

$$p_{i,id} = \sum_{j=1}^{K} \frac{p_{ij,id}}{\omega_j} \Bigg/ \sum_{j=1}^{K} \frac{1}{\omega_j} \tag{2}$$

3.1. Modelling of the indentation test

The finite element simulation of the indentation test was carried out using the commercial code Abaqus (see [25]). Due to the axial symmetry of the indenter and the absence of anisotropy of tested specimen, the indentation test was simulated by 2D axially-symmetric numerical model with 14,800 quadrilateral finite elements and 28,000 DOFs approximately. The indenter was modelled as rigid analytical, which represented a reasonable assumption given the sharp opening angle of it. The adopted mesh for the simulations is illustrated in Fig. 3.

The material constitutive model adopted assumes the existence of an initial linear-elastic range followed, beyond the yield limit, by the classical Hencky-Huber-von Mises (HHM) plasticity model with exponential isotropic hardening. The inelastic material properties are fully characterized by the two constants f_y and n, which represent yield stress and exponential hardening parameter, respectively. For the materials considered in this paper (i.e. metals), it is reasonable to assume that, locally in a large strains regime, plastic strains are much larger than the elastic ones and as a well-known consequence, to assume additivity of the two parts (see Ref. [26]).

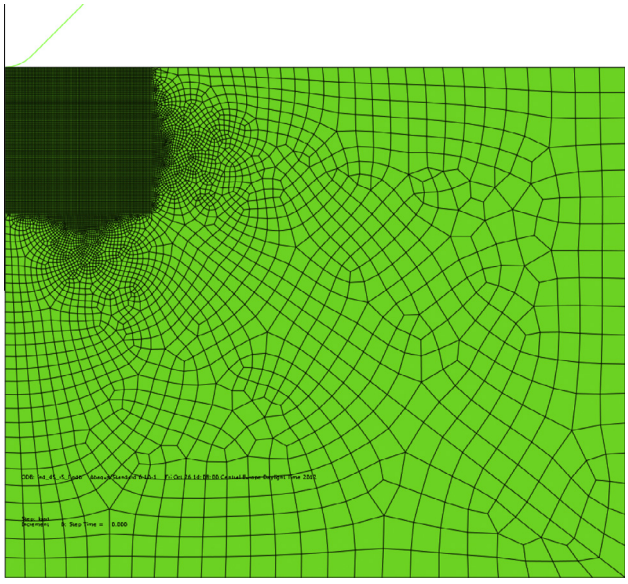

Fig. 3. Finite element mesh used for the indentation test simulations.

This constitutive law is appropriate for the class of materials, i.e. aluminium alloys, considered in the experimental part of this study and it can be formulated, in terms of true stress and true strain quantities, as follows:

$$\dot{\varepsilon}_{ij} = \dot{\varepsilon}^{el}_{ij} + \dot{\varepsilon}^{pl}_{ij} \tag{3}$$

$$\dot{\sigma}_{ij} = D_{ijkl}\dot{\varepsilon}^{el}_{kl} \tag{4}$$

$$\dot{\varepsilon}^{pl}_{ij} = \dot{\lambda}\frac{\partial f}{\partial \sigma_{ij}} \tag{5}$$

$$f(\sigma_{ij}) = \sqrt{\frac{3}{2}s_{ij}s_{ij}} - \sigma_0(\varepsilon^{pl}_{eq}) \tag{6}$$

$$\sigma_0(\varepsilon^{pl}_{eq}) = f_y \left(\frac{E}{f_y}\right)^n \left(\frac{f_y}{E} + \varepsilon^{pl}_{eq}\right)^n \tag{7}$$

$$\varepsilon^{pl}_{eq}(T) = \int_0^T \sqrt{\frac{2}{3}\dot{\varepsilon}^{pl}_{ij}(\tau)\dot{\varepsilon}^{pl}_{ij}(\tau)}\,d\tau \tag{8}$$

in which ε_{ij} represent the strain tensor components decomposed into the elastic ε^{el}_{ij} and plastic ε^{pl}_{ij} components; D_{ijkl} is the fourth-order isotropic elastic tensor; $f(\sigma_{ij})$ is the yield function which defines the current elastic domain and the direction of the plastic strains according to an associated flow rule; λ represents the plastic multiplier; s_{ij} are the deviatoric stress tensor components and $\sigma_0(\varepsilon^{pl}_{eq})$ represents the current yield stress defined as function of the equivalent plastic strain ε^{pl}_{eq} according to an exponential isotropic hardening rule, which depends on the inelastic parameters f_y and n.

The proposed parameter characterization approach relied on the minimization of the discrepancy function defined by Eq. (1). The adopted optimization algorithm is iterative and requires repetitive computations of the system response (i.e. numerical generation of indentation curves and maximum pile-up height) for various different vectors of parameters $\mathbf{p}$. Due to the non-linearities present in the numerical model (material, geometrical and contact between indenter and indented material), the procedure is extremely lengthy (because computationally demanding) if at each iteration the response of the system to the indentation test has to be computed with a finite element model. To overcome this inconvenience, the numerical calculations were performed by a reduced basis technique based on Proper Orthogonal Decomposition (POD) and Radial Basis Functions (RBF), described in the following Section.

3.2. POD–RBF technique for indentation test modelling

In practical problems of parameter estimation, it is common to require numerous estimations of response of the same system (same in terms of geometry, boundary conditions, external actions etc) corresponding to different parameter values. Variation of parameters in this context generates "correlated" changes of the measurable quantities in the system response. "Correlation" here means that, assuming the measurable quantities in each experiment simulation be represented by a vector (called "snapshots" in pertinent jargon), these vectors are going to be "correlated" or almost parallel in their space. Such correlation naturally suggests to change the reference axes in the space of snapshots so that

snapshot projections on some of the new axes can be neglected because exhibiting a relatively small norm. A mathematical technique which is used to find new orthogonal directions, for which the error of approximation introduced by the above-mentioned removal of certain axes is minimized, is called Proper Orthogonal Decomposition (POD). For completeness, a brief outline of the applied steps involved in the use of POD in the present context, is provided in the following, while for a detailed treatment of the approach reference should be made to specialised literature (e.g. see [27,28]):

(i) Let the $N \times Q$ matrix $\mathbf{U}$ gather the above-mentioned snapshots $\mathbf{u}_i$, with $i = 1...Q$, each of them collecting N measurable quantities resulting from FE simulations, based on Q parameter combinations.

(ii) The symmetric, positive-semi-definite matrix $\mathbf{D}$ is generated from the snapshot matrix as $\mathbf{D} = \mathbf{U}^T \cdot \mathbf{U}$. The eigenvalue problem of matrix $\mathbf{D}$ is further solved, and the new basis is constructed with orthogonal directions defined by:

$$\mathbf{\Phi} = [\boldsymbol{\varphi}_1 \quad \dots \quad \boldsymbol{\varphi}_N], \quad \boldsymbol{\varphi}_i = \mathbf{U} \cdot \mathbf{v}_i \cdot \lambda_i^{-1/2}, \quad (i = 1, \dots N), \quad \mathbf{\Phi}^T \cdot \mathbf{\Phi} = \mathbf{I} \tag{9}$$

where $\mathbf{v}_i$ is the eigenvector and λ_i the corresponding eigenvalue of matrix $\mathbf{D}$.

(iii) It is analytically demonstrated (see e.g. [28]) that such basis represents an optimal basis for the approximation of the snapshot matrix $\mathbf{U}$, in a sense that by keeping only the first fixed number of directions, say $\bar{N}$ of them, there will be no better $\bar{N}$-component approximation of the snapshots collected in matrix $\mathbf{U}$. Therefore, low-order approximation of previously generated system responses is computed by:

$$\mathbf{U} \approx \bar{\mathbf{\Phi}} \cdot \bar{\mathbf{A}} \tag{10}$$

with $\bar{\mathbf{A}}$ called matrix of truncated amplitudes, or projections of the snapshots to the sub-space spanned by $\bar{\mathbf{\Phi}}$, defined as the first $\bar{N}$ orthogonal directions calculated by Eq. (9).

(iv) To have a continuous approximation of the system response, Radial Basis Functions (RBF) are used to interpolate the amplitudes and to establish one interpolation function valid for the whole parameter space. The vector of amplitudes becomes then a function of parameters and can be written as:

$$\bar{\mathbf{a}}(\mathbf{p}) = \sum_{i=1}^{Q} \mathbf{b}_i \cdot g_i(\mathbf{p}) \tag{11}$$

with $1 \times \bar{N}$ $\mathbf{b}_i$ vectors collecting interpolation coefficients, to be defined later, and g_i radial basis functions adopted for the interpolation, which in general form can be expressed as:

$$g_i(\mathbf{p}) \equiv g_i(\|\mathbf{p} - \mathbf{p}_i\|), \quad i = 1, \dots Q \tag{12}$$

(v) Coefficients of interpolation are computed by imposing Eq. (11) for all Q pairs of parameters and corresponding truncated amplitudes, which results in the following system of linear equations:

$$\bar{\mathbf{A}} = \mathbf{B} \cdot \mathbf{G} \tag{13}$$

(vi) Once matrix $\mathbf{B}$ is calculated, for any arbitrary combination of parameters, the system response is computed by combining Eqs. (10) and (11), namely:

$$\mathbf{u}(\mathbf{p}) \approx \bar{\mathbf{\Phi}} \cdot \mathbf{B} \cdot \mathbf{g}(\mathbf{p}) \tag{14}$$

The above sequence of steps, which needs to be performed only once for a particular application, results in the calibration of matrices $\bar{\mathbf{\Phi}}$ and $\mathbf{B}$. For any further calculation of indentation curves and residual imprint, corresponding to an arbitrary parameter combination, it is required to compute only vector $\mathbf{g}$, and to perform the matrix multiplication of Eq. (14). This approximation of the test response is clearly computed much faster than the finite element simulation, while the error remains on the same level, as it will be demonstrated further on. The use of this approach contributes to a significant reduction of overall computing time spent for the assessment of the sought parameters.

In the 3-dimensional space of the sought parameters, the "search domain" was defined through the lower and upper bounds adopted for each parameter (see Table 3). The above-mentioned snapshots $\mathbf{u}_i$ were computed with respect to a regular grid obtained by subdividing each interval in a certain number of subintervals. Alternative approaches based on randomness, might be required in other applications. For the purpose of this study, the calibration of the reduced basis model was carried out with $Q = 1700$ material parameters' combinations within the ranges contained in Table 3. This required an overall computing CPU time of approximately 200 h on a computer with processor i5 and 6 GB of RAM. From each analysis, 50 penetration depths corresponding to 50 load levels were taken from the loading part of the indentation curve as well as from its unloading branch. In addition, 50 points with corresponding x–y coordinates were taken from the pile-up region and this data was collected within the snapshot vector $\mathbf{u}$, subsequently approximated by the above described procedure (i.e by Eq. (14)). The basis for the snapshot matrix (collecting above mentioned vectors $\mathbf{u}$) was truncated after the seventh new reference direction (i.e. $\bar{N} = 7$), satisfying the accuracy criterion of reducing to less than 10^{-6} the ratio between the summation of neglected eigenvalues and the summation of all of them. References included in [27] should be considered for more information on the accuracy criteria of POD reduced basis models. For the RBF interpolation the following function was adopted:

$$g_i(\mathbf{p}) = \|\mathbf{p} - \mathbf{p}_i\|^3 \tag{15}$$

The accuracy of the POD model is highlighted in Fig. 4(a and b), which presents a comparison between the response of the system to an indentation test computed by means of both the finite element model implemented in Abaqus and the POD model. These results are expressed in terms of indentation curve and imprint geometry, adopting a set of material parameters not belonging to the Q parameter combinations used in the calibration stage. While the two responses are identical there is a significant difference in terms of numerical efficiency, which is clearly expressed by the fact that the POD model required a fraction of a second of CPU time to compute the response on a computer with processor i5 and 6 GB of RAM, against the 15 minutes taken by the Abaqus finite element model on the same PC. Obviously, the gain in computing time becomes more pronounced the longer the inverse analysis has to run for.

4. Validation of the pod based identification procedure

The inverse analysis procedure proposed in Section 3 is validated in the following against the experimental results reported

Table 3
Domain of interest considered for the parameter space of the POD–RBF indentation test modelling.

	Min	Max
E	50 GPa	120 GPa
f_y	25 MPa	120 MPa
n	0.015	0.300

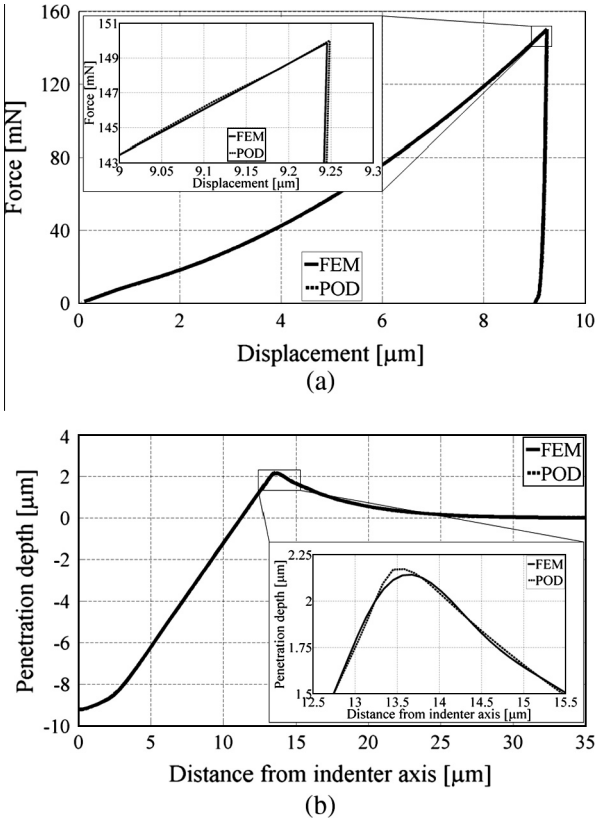

Fig. 4. Comparison between indentation curve (a) and imprint geometry (b), computed by means of the finite element model implemented in Abaqus (FEM) and by means of the POD model, adopting E = 79 GPa; f_y = 70 MPa, and n = 0.06.

in Section 2 to highlight the efficiency and the robustness of the proposed approach to estimate both elastic and inelastic material properties for the constitutive law expressed by Eqs. 3–8.

For each material considered in this study there were two sources of information collected independently during the experimental work, which consisted of: (i) the nominal stress–strain curves obtained from tensile tests, used for the benchmarking of the indentation-based characterization procedure, and (ii) the indentation curves with the additional information of the maximum pile-up heights, included as input in the inverse analysis procedure.

4.1. Characterization of the benchmarking material properties obtained from tensile tests

For the validation of the inverse analysis approach, it is essential to accurately estimate the values for the modulus of elasticity E, the yield stress f_y and the exponential hardening parameter n from the tensile test measurements. While a trial and error procedure is sound in principle, it might not enable a unique identification of the parameters, especially when dealing with constitutive models such as those described in Eqs. 3–8, as it is possible to achieve slightly different combinations of the material parameters which adequately predict the experimental curves. It is worth pointing out that the inelastic material parameters measured directly from the experimental curves, expressed in term of nominal quantities, such as those reported in Table 1, cannot be compared with those resulting from the proposed inverse procedure, the latter being based on a constitutive law defined in terms of true quantities.

In the present study, an additional inverse analysis problem was solved to estimate the material parameters from the tensile test results. In the first step, the elastic modulus E was identified as the slope of the stress–strain curve in its initial loading range, i.e. for stress levels below 30% of the peak stress measured. Then the best estimate of the sought inelastic parameters, i.e. f_y and n, entering the true stress–strain curve expressed by Eq. (7), was found by minimizing the discrepancy between experimental and computed quantities, expressed in terms of the area under the nominal stress–strain curve. In this process, the following relationships between the true stress σ_0 and true plastic strain ε_{eq}^{pl}, required in Eq. (7), and the corresponding nominal stress S and nominal total strain M measured from the tensile tests, were adopted:

$$S = \frac{\sigma_0(\varepsilon_{eq}^{pl})}{\exp\left(\varepsilon_{eq}^{pl} + \frac{\sigma_0(\varepsilon_{eq}^{pl})}{E}\right)} \tag{16a}$$

$$M = \exp\left(\varepsilon_{eq}^{pl} + \frac{\sigma_0(\varepsilon_{eq}^{pl})}{E}\right) - 1 \tag{16b}$$

The elastic modulus was identified separately because, by including all three parameters (E, f_y and n) in the above inverse analysis procedure, the value obtained for the elastic modulus was mainly governed by the discrepancies between the inelastic parts of the numerical and experimental stress–strain curves and, therefore, did not match well the initial slope of the curve.

The curves and values identified with this process have been plotted in Figs. 5 and 6, and reported in Table 4. These were used for the benchmarking of the inverse analysis procedure as outlined in the following Section.

4.2. Inverse analysis procedure applied to indentation test results

The inverse analysis approach described in Section 3 is here applied for the characterization of the material properties for the AA 6061-O and AA 7075-O samples presented in Section 2. The best estimate of the sought parameters is evaluated by minimizing the discrepancy between the experimental results (indentation curve and maximum pile-up height) and the outcomes of the POD model (Section 3.2), relying on the constitutive law described by Eqs. 3–8. The nominal stress–strain curve is then determined using Eqs. (16a) and (16b). In this study, the experimental indentation curves and maximum pile-up heights, used for the inverse analysis, were taken as the average of the measured ones for each material considered.

Fig. 5 illustrates the nominal stress–strain curves for the AA 6061-O alloy that were determined based on: (i) experimental tensile tests, (ii) inverse analysis applied to the tensile tests, and (iii) inverse analysis carried out on the indentation tests. All curves

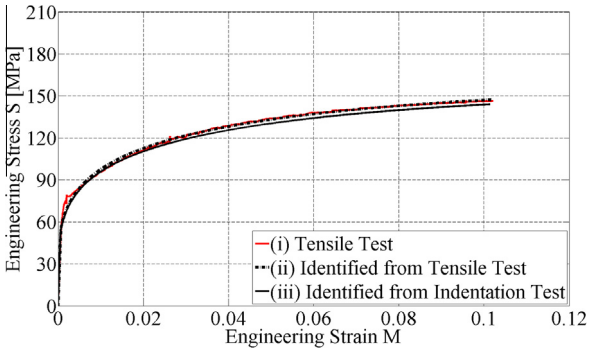

Fig. 5. Nominal stress strain curves for material AA 6061 obtained from: (i) experimental tensile tests, (ii) characterization from tensile test results based on Eq. (7) and (iii) inverse analysis carried out on indentation tests.

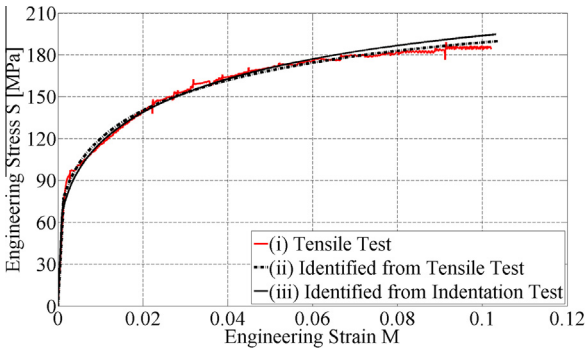

Fig. 6. Nominal stress strain curves for material AA 7075 obtained from: (i) experimental tensile tests, (ii) characterization from tensile test results based on Eq. (7) and (iii) inverse analysis carried out on indentation tests.

Table 4
Material parameters identified from the tensile test results (characterized using Eq. (7)) and from the indentation tests.

Specimen	Properties	From tensile tests	From indentation tests	Difference (%)
AA 6061-O	E (MPa)	97,405	99,151	+1.7
	f_y (MPa)	53.4	52.1	−2.4
	n	0.215	0.214	−0.4
AA 7075-O	E (MPa)	64,640	66,848	3.4
	f_y (MPa)	74.5	67.2	−9.7
	n	0.234	0.255	8.9

are shown to match well. Good results were also observed for the AA 7075-O alloy samples, as depicted in Fig. 6.

The agreement between the experimental curves and their best-fitting through Eqs. (7), (16a) and (16b) shows that the material model adopted in this study is able to interpret correctly the material behavior of the AA 6061-O and AA 7075-O alloys.

The good results with the proposed inverse analysis approach are also highlighted in Table 4, where the material parameters, related to the true stress–strain curves, identified from both the experimental tensile and indentation tests by means of the inverse analysis procedures adopted, are compared, and the differences between the two sets of results are expressed as a percentage.

For the AA 6061-O alloy, the maximum difference between the identified and tensile test parameters was equal to −2.4%, calculated for the yield stress f_y. Smaller differences were noted for the elastic modulus E (+1.7%) and the exponential hardening parameter n (−0.4%). Larger errors were observed for the AA 7075-O alloy, with maximum difference of −9.7% still exhibited for the yield stress f_y. The remaining errors were 3.4% and 8.9%, calculated for the elastic modulus E and the exponential hardening parameters n, respectively.

5. Conclusions

The use of instrumented indentation has been gaining popularity in recent years for the characterization of the material properties, for industrial and scientific applications, thanks to its non-invasive nature. This paper presented and validated a methodology aimed at enhancing the computational efficiency of the inverse analysis procedure for the characterization of metallic material properties. This was carried out by implementing a computationally efficient approach to simulate the response of the material when subjected to an indentation test by using an 'a priori' model reduction procedure, developed with a POD scheme. The POD model was calibrated with a finite element model implemented in the commercial software Abaqus. The input data specified for the inverse analysis made use of the indentation curves and maximum pile-up heights left on the sample at the completion of the indentation tests. The accuracy of the numerical procedure was validated against the experimental results recorded for aluminium alloys AA 6061-O and AA 7075-O specimens. Benchmarking values for the material properties were obtained from tensile tests carried out independently from the indentation tests on the same metallic samples. The overall procedure was shown to lead to good estimates of the material properties required for the characterization of the aluminium alloys considered in this study.

Acknowledgements

The work in this article was supported by the Australian Research Council through its Discovery Projects funding scheme (DP1096454) and by an award under the Merit Allocation Scheme on the NCI National Facility at the ANU. Support from the University of Sydney (Materials & Structures Research Cluster) is gratefully acknowledged. Part of the computational services used in this work was provided by Intersect Australia Ltd.

References

[1] W.C. Oliver, G.M. Pharr, J. Mater. Res. 7 (1992) 176–181.
[2] G. Bolzon, G. Maier, M. Panico, Int. J. Solids Struct. 41 (2004) 2957–2975.
[3] Y. Gu, T. Nakamura, L. Prcklik, S. Sampath, J. Wallace, Mater. Sci. Eng. 345 (2003) 223–233.
[4] M. Bocciarelli, G. Maier, Comput. Mater. Sci. 39 (2007) 381–392.
[5] V. Buljak, G. Maier, Eng. Struct. 33 (2011) 492–501.
[6] N. Dao, N. Chollacoop, K.J. van Vliet, T.A. Venkatesh, S. Suresh, Acta Materalia 49 (2001) 3899–3918.
[7] M. Bocciarelli, G. Bolzon, G. Maier, Mech. Mater. 37 (2005) 855–868.
[8] K. Matsuda, Philos. Mag. A 82 (2002) 1941–1951.
[9] O. Jorgensen, A.E. Giannakopoulos, S. Suresh, Int. J. Solids Struct. 58 (1998) 505–513.
[10] J.G. Swadener, J.-Y. Rho, G.M. Pharr, J. Biomed. Mater. Res. 57 (2001) 108–112.
[11] M.A.J. Cox, N.J.B. Driessen, R.A. Boerboom, C.V.C. Bouten, F.P.T. Baaijens, J. Biomech. 41 (2008) 422–429.
[12] A. Gatto, J. Mater. Process. Technol. 174 (2006) 67–73.
[13] A. Meneses-Amador, I. Campos-Silva, J. Martínez-Trinidad, S. Panier, U. Figueroa-López, A. Torres-Hernández, Surf. Coat. Technol. 215 (2013) 285–290.
[14] X. Chen, N. Ogasawara, M. Zhao, N. Chiba, J. Mech. Phys. Solids 55 (2007) 1618–1660.
[15] C.K.S. Moy, M. Bocciarelli, S.P. Ringer, G. Ranzi, Mater. Sci. Eng., A 529 (2011) 119–130.
[16] R. Fedele, M. Filippini, G. Maier, Comput. Struct. 83 (2005) 1005–1020.
[17] G. Bolzon, V. Buljak, Fatigue Fract. Eng. Mater. Struct. 34 (2011) 97–107.
[18] C. Moy, M. Weiss, J. Xia, G. Sha, S.P. Ringer, G. Ranzi, Mater. Sci. Eng., A 552 (2012) 48–60.
[19] AS 1391-2007: Metallic materials – Tensile testing at ambient temperature. 2007: Australian Standard.
[20] J. Alkorta, J.M. Martinez-Esnaola, J.G. Sevillano, J. Mater. Res. 20 (2005) 432–437.
[21] M. Bocciarelli, G. Bolzon, G. Maier, Comput. Mater. Sci. 43 (2008) 16–26.
[22] M. Bocciarelli, G. Bolzon, Int. J. Fract. 155 (2009) 1–17.
[23] J. Nocedal, S.J. Wright, Numerical Optimization, Springer – Verlag, New York, 2006.
[24] MATLAB. User's guide and optimization toolbox, release 6.13, The Math Works Inc., USA, 2002.
[25] HKS Inc, Pawtucket, RI, USA. ABAQUS/Standard, Theory and User's Manuals, release 6.10.
[26] I. Doghri, Mechanics of Deformable Solids, Springer Verlag, Berlin, 2000.
[27] V. Buljak, Inverse Analysis With Model Reduction – Proper Orthogonal Decomposition in Structural Mechanics, Springer Verlag, Berlin, 2012.
[28] A. Chatterjee, Curr. Sci. 78 (2000) 808–817.